IEEE Access
Multidisciplinary | Rapid Review | Open Access Journal

Received 10 October 2023, accepted 8 November 2023, date of publication 16 November 2023,
date of current version 29 November 2023.

*Digital Object Identifier 10.1109/ACCESS.2023.3334161*

RESEARCH ARTICLE

# High-Definition Plane-Wave Ultrasound Imaging Based on Subbands Phase Information Extracted From Echo Signals

**JIE ZHENG[1], JING ZHU[2], AND NORIO TAGAWA[1], (Member, IEEE)**
[1]Graduate School of Systems Design, Tokyo Metropolitan University, Tokyo 191-0062, Japan
[2]Research Center for Humanoid Sensing, Zhejiang Lab, Hangzhou 311100, China

Corresponding author: Jie Zheng (zheng-jie@ed.tmu.ac.jp)

**ABSTRACT** We have been studying high-definition ultrasound imaging based on phase information of subband components extracted from received echoes. We address coherent imaging with array transducers based on plane wave transmission. Coherent imaging can be realized algebraically or analytically based on modeling the received signal as a convolution of reflected waves from scatterers. Receive Beam-Forming, on the other hand, has been effectively used as an approximate method to reduce computational complexity. For both above-mentioned coherent imaging schemes, we have proposed high resolution imaging approaches based on the extraction of subband components from the received signal, respectively, in order to effectively utilize the phase information of the echoes. In this study, we propose a super resolution imaging method that integrates both approaches and is specifically designed for application to medical diagnosis. We confirm the performance of the proposed method through a series of experiments on phantom and biological images.

**INDEX TERMS** Super resolution, plane wave beam-forming, phase information, range MUSIC, adaptive compound.

## I. INTRODUCTION

The inferior image quality of ultrasound imaging in comparison to X-ray CT and MRI necessitates attention. In recent decades, there have been many research endeavors aimed at improving resolution and contrast, reducing unwanted interferences and artifacts [1], [2], [3].

The imaging methods utilizing pulsed ultrasound for transmission and reception can be categorized into two general schemes. One scheme models the received echo as a convolution of the transmitted pulse wave and multiple scatterer reflectances to accurately detect scatterer position. Time-Reversal MUltiple SIgnal Classification (TR-MUSIC) is a typical example of this scheme [4]. Utilizing the principle that echoes received at each element converge on a scatterer when they are time-reversed and retransmitted, TR-MUSIC detects the received phase generated by a real scatterer at each element and achieves lateral super-resolution through MUSIC calculation [5].

Another scheme that cancels incoherent echoes and images the scatterer target clearly is Receive Beam Forming (RBF). This is done by summing the received signals of the array elements together with matching delays, without using a model of the received signal explicitly. The Minimum-Variance RBF (MV-RBF) [6], Filtered-Delayed Multiply And Sum (FDMAS) [7], and Generalized Coherence Factor (GCF) [8] are essential in current clinical applications. The MV-RBF enables improvement of resolution primarily in the lateral direction through the determination and use of adaptive weights when adding individual element echoes [9]. Both FDMAS and GCF use the degree of coherency of the received echoes being added together to enhance contrast by suppressing unwanted interference [10], [11].

Taking into account the aforementioned principles, our research aims to examine imaging techniques that make use of the phase information in echo waveforms to enhance

The associate editor coordinating the review of this manuscript and approving it for publication was Riccardo Carotenuto.

spatial resolution and reduce artifacts caused by undesirable interference [12], [13], [14], [15], [16]. Specifically, this study explores coherent imaging utilizing plane-wave pulse transmission, with the assumption of array transducers.

We have proposed two primary techniques. The first one aims to achieve a high-resolution scatterer position and reflectivity detection by using the received signals from each transducer element or their received beam-formed line signals. These signals are modeled as a convolution of echoes from multiple scatterers [17], [18], which belongs to the former scheme described above. This technique employs the phase characteristic of echoes from scatterers at a distance of $z$ from the transducer, expressed as $\theta_f = 2\pi fz$. Echoes from various locations of scatterers can be differentiated by their frequency dependence on $\theta_f$. This enables high-resolution detection of scatterers and is known as the Range-MUSIC (R-MUSIC) within this article. A complex signal subspace can be constructed based on subband echoes with varying center frequencies. As mentioned earlier, the difference in phase rotation speed with frequency ensures that the signal subspace's dimensions correspond to the number of scatterers at different distances.

Another proposed technique utilizes phase information within the framework of the RBF to effectively eliminate off-axis echoes, allowing for high-resolution imaging [19], [20]. Off-axis echoes are echoes from locations other than the target and removing them is of utmost importance. Multiple sub-band echo phases are out of sync with the off-axis echo component due to delayed sampling with respect to the pixel of interest, making this technique useful in reducing off-axis echoes. The techniques developed based on this principle are identified as the Adaptive Sub-Band Compounding (A-SBC) in this paper.

In this study, we propose a new technique for obtaining high-resolution images by integrating R-MUSIC and A-SBC, which makes use of subband phase information. In summary, we utilize R-MUSIC on the obtained signal of each element separately and combine the results using A-SBC as RBF. The dual use of sub-band phase information results in an improvement of the resolution, especially in the range direction. The R-MUSIC-based method requires synthetic aperture imaging. However, no special technical innovations have been made for multiple transmissions. This study proposes a method that integrates R-MUSIC results from each transmission at different transmission angles with the A-SBC-based method. This integration improves resolution and suppresses unwanted interference.

The contributions of this study can be summarized as follows:

1) Enhancement of range resolution is accomplished by utilizing phase information from subbands through R-MUSIC and A-SBC techniques.
2) Apply the R-MUSIC technique using plane waves that are transmitted and received in various directions to enhance the imaging of multiple scatterers at high resolution.

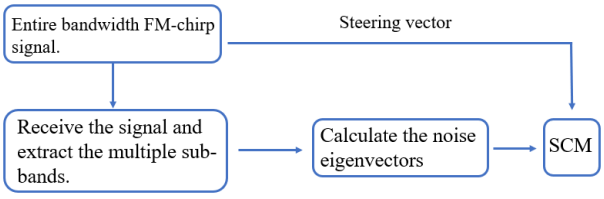


**FIGURE 1.** Flowchart of the calculation of SCM.

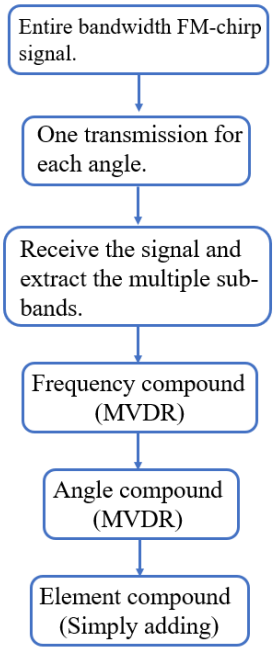


**FIGURE 2.** Flowchart of filtered-FPWC-MVDR.

3) To achieve high resolution and contrast, we use a combination of R-MUSIC and CF imaging techniques. We reconsider three critical components of RBF, namely transmission angle, sub-band, and element.
4) Instead of transmitting the signal repeatedly in the same direction, both R-MUSIC and A-SBC use filters to extract subbands. This reduces the number of transmissions needed and makes the proposed method comparable to coherent plane-wave compounding (CPWC). CPWC transmits the signal as a multi-angle plane wave and beamforms the received echoes at each angle using the Delay-and-Sum (DAS) method. Finally, the proposed method is also practical as it incorporates DAS values from various angles, which have been widely used in ultrasound research and clinical settings [21].

## II. METHODS

### A. METHODOLOGY UNDERLYING THIS STUDY

This section outlines our previous R-MUSIC and A-SBC approaches and proposes an integrated technique.

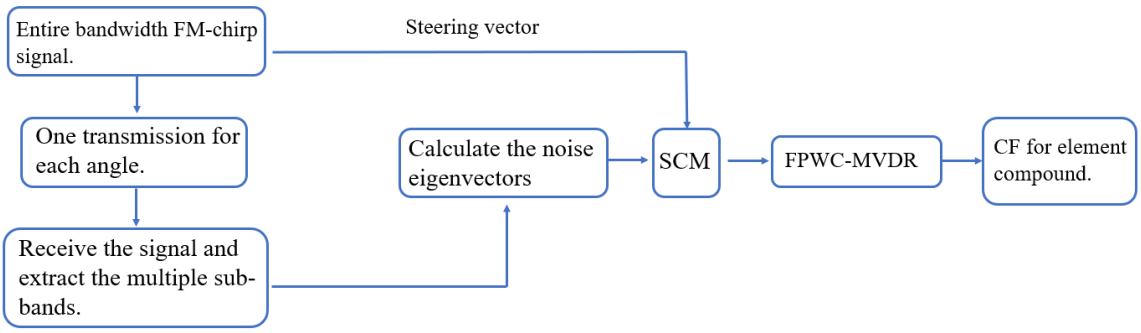


**FIGURE 3.** Flowchart of the proposed method.

R-MUSIC is based on the MUSIC algorithm, which uses the noise subspace obtained by subtracting the signal subspace from the total function space of the echo [22], [23]. Several methods have been proposed to achieve R-MUSIC by using FM chirp pulses to attain a high Signal-to-Noise Ratio (SNR). One specific method is the Super Resolution FM-Chirp Correlation Method (SCM) [24]. SCM relies on focused beam transmission. Additionally, the Synthetic Aperture-SCM (SA-SCM) has been introduced, utilizing divergent-wave transmission and applying SCM to the received signal of each transducer element. A reduction in the number of transmissions and receptions has been achieved by this method [25]. Subsequently, we developed a technique called the SCM-weighted SA [26] which implements the SCM profile signal as an apodization function to improve imaging quality in the axial direction. To further enhance the resolution, the SCM-weighted SA-SCM was implemented, whereby SCM was reapplied to each image line for the subband images obtained by SCM-weighted SA [27].

As a specific implementation of A-SBC method, we use plane-wave coherence RBF and introduce a new one called the Frequency and Plane-Wave Compounding Minimum Variance Distortion-Free Response (FPWC-MVDR) [28]. This approach combines subbands with transmission angle compounding, which is utilized in the conventional Data-Compounded-on-Receive MVDR (DCR-MVDR) approach [29]. Angle compounding is a technique that adjusts the transmission angle to modify the mixing time of echoes from off-axis, causing phase mismatch to nullify their effects on the received signal. This technique generally leads to improved resolution in the lateral direction. However, subband compounding, by altering the frequency, can induce phase mismatch off the axis and produce resolution enhancement primarily in the range direction. To obtain subband echoes, we previously transmitted and received pulses in separate subbands multiple times. However, we have verified that subband components can be extracted from a single received signal acquired using a digital filter on a wideband pulse transmission. This method, known as the filtered FPWC-MVDR [30], has been confirmed to produce the intended outcomes. Combining multiple sub-band components produces identical output as processing an undecomposed received signal. For refined image quality, working on a pixel-specific level is crucial [31], [32]. In both FPWC-MVDR and filtered FPWC-MVDR methods, MV compounding technique was utilized for subband and angle compounding to improve resolution [28], [30], [33]. To avoid unwanted interference, the use of the CF coefficients [34], [35], [36], [37] could be applied for adaptive compounding. For compounding transducer elements, either the MV method or CF imaging can be used, although DAS is more convenient for simplicity.

In this study, in order to integrate R-MUSIC and A-SBC, we multiply the SCM results obtained from each array element as weights with subbands, and then the subbands with the SCM weights are subjected to FPWC-MVDR beamforming. To suppress unwanted interference, CF coefficients could be utilized for element compound. Finally, in order to ensure the timeliness, both SCM and FPWC-MVDR use the method that the entire effective bandwidth signal is transmitted only once, and the received echoes are extracted from several subbands of different frequencies using bandpass filters. A flowchart of SCM using filters is shown in Fig. 1, and Fig. 2 illustrates the process flow of FPWC-MVDR using filters. Fig. 3 shows the flowchart of the proposed method.

### B. PRINCIPLE AND OUTLINE OF SCM

The MUSIC algorithm is a widely used technique within the eigenspace-based class [38]. It partitions the eigenspace associated with the covariance matrix of the initial channel data into noise and signal subspaces, incorporating knowledge of the noise covariance. It then calculates the direction of signal arrival. R-MUSIC is an extended version of MUSIC and is applied from the array element direction to the time axis direction. R-MUSIC removes limitations on the transmitter waveform's usage. SCM, a variant of R-MUSIC, employs an FM chirp signal as its transmitter waveform.

The transmitted FM chirp signal $s(t)$ with a center frequency of $\omega_0$ is denoted by

$$s(t) = \mathrm{Re}\left[a(t)e^{j\omega_0 t}\right]. \tag{1}$$

The echo signal, denoted as $b(t)$, generated by $D$ point scatterers can be formulated as

$$b(t) = \int_{-\infty}^{\infty} h(\tau)s(t-\tau)\,d\tau, \tag{2}$$

where the impulse response $h(t)$ can be expressed using the complex reflection coefficient of each scatterer $h_i$ and the delay time $\tau_i$ as follows:

$$h(t) = \sum_{i=1}^{D} h_i \delta(t-\tau_i). \tag{3}$$

The Dirac delta function is denoted by $\delta(\cdot)$. The baseband In-phase / Quadrature phase (IQ) representation of the received signal, $v(t)$, and its compressed signal, $c(t)$, are formulated as follows:

$$v(t) = \sum_{i=1}^{D} h_i a(t-\tau_i)e^{-j\omega_0\tau_i} + n(t), \tag{4}$$

$$c(t) = \sum_{i=1}^{D} h_i r(t-\tau_i)e^{-j\omega_0\tau_i} + m(t), \tag{5}$$

where $r(t)$ represents the complex autocorrelation function of $a(t)$ in the baseband. The observed noise, $n(t)$, is assumed to be white Gaussian noise with variance $\sigma^2$, and $m(t)$ is the cross-correlation of $a(t)$ and $n(t)$ with complex values. When using a short pulse instead of an FM chirp as the transmit wave, we can refer to Eq. 5, where $c(t)$ is the received signal and $r(t)$ is the transmit pulse. The noise, $m(t)$, is obviously white Gaussian noise.

The discrete representation of $c(t)$ with $P$ sampling points is denoted as $c \equiv [c(t_1), c(t_2), \ldots, c(t_P)]^\top$. The steering vector $\mathbf{r}_i$ can be defined as $\mathbf{r}_i \equiv [r(t_1-\tau_i), r(t_2-\tau_i), \ldots, r(t_P-\tau_i)]^{\mathrm{T}}$, and the noise vector is represented as $\mathbf{m} \equiv [m(t_1), m(t_2), \ldots, m(t_P)]^\top$. Therefore, $\mathbf{c}$ can be expressed as follows:

$$\mathbf{c} = \sum_{i=1}^{D} h_i e^{-j\omega_0\tau_i}\mathbf{r}_i + \mathbf{m}. \tag{6}$$

By defining the scatterer reflectivity vector $\mathbf{g} \equiv [h_1 e^{-j\omega_0\tau_1}, h_2 e^{-j\omega_0\tau_2}, \cdots, h_D e^{-j\omega_0\tau_D}]^\top$ and the steering matrix $\Gamma \equiv [\mathbf{r}_1, \mathbf{r}_2, \cdots, \mathbf{r}_D]$, the following equation can be derived for $\mathbf{c}$:

$$\mathbf{c} = \Gamma\mathbf{g} + \mathbf{m}. \tag{7}$$

The variance covariance matrix $\mathbf{R} = E\{\mathbf{c}\mathbf{c}^{\mathrm{H}}\}$ of $\mathbf{c}$ can be expressed as:

$$\mathbf{R} = \Gamma\mathbf{G}\Gamma^{\mathrm{H}} + \mathbf{R}_m, \tag{8}$$

where $\mathbf{G} \equiv E[\mathbf{g}\mathbf{g}^{\mathrm{H}}]$ and $\mathbf{R}_m \equiv E[\mathbf{m}\mathbf{m}^{\mathrm{H}}] = \sigma^2\mathbf{R}_0$ with a Hermitian matrix $\mathbf{R}_0$ whose $kl$-th element is $r(t_k - t_l)$. The notation $E[\cdot]$ represents the expectation operator and $\cdot^H$ denotes the conjugate transpose. It is evident that the echoes and observation noise are statistically independent, enabling the general eigenvalue problem to be considered.

$$\mathbf{R}e_i = \lambda_i\mathbf{R}_0 e_i, \qquad i = 1, 2, \ldots, P. \tag{9}$$

The eigenvalues of $P$ are arranged in descending order. The eigenvectors $\{\mathbf{e}_i\}_{i=1}^{D}$ that correspond to the first through the $D$-th eigenvalue greater than $\sigma^2$ define the signal subspace. The eigenvector $\{\mathbf{e}_i\}_{i=D+1}^{P}$ with smaller eigenvalues acts as the foundation of the noise subspace. The signal and noise subspaces are orthogonal complements.

While adjusting the delay time position of the steering vector, a super-resolution delay profile $S(t_i)$ is computed for each delay time using the computational principles of MUSIC.

$$S(t_i) = \frac{\mathbf{r}_i^{\mathrm{H}}\mathbf{R}_0^{-1}\mathbf{r}_i}{\sum_{j=D+1}^{P}|\mathbf{r}_i^{\mathrm{H}}\mathbf{e}_j|^2}. \tag{10}$$

If $\mathbf{R}$ is estimated by averaging multiple received signals within the same frequency band, the eigenvalues are likely to be reduced almost to one. As a result, a single eigenvector, namely the basis of the signal subspace, is determined. Even when there are multiple echoes requiring separation in the received signal, this phenomenon persists. In order to avoid this issue, R-MUSIC performs $\mathbf{R}$ estimation by averaging multiple received signals within different subbands. The phase rotation resulting from the change in frequency of an echo is directly proportional to the distance of the scatterer. To separately obtain eigenvalues and eigenvectors corresponding to echoes of scatterers at different distances, various subbands are utilized. Our previous study builds on this foundation by randomly changing the frequency band for multiple transmissions and receptions. The ensemble average of $\mathbf{R}$ is subsequently estimated as

$$\hat{\mathbf{R}} = \frac{1}{L}\sum_{j=1}^{L}\mathbf{c}_j\mathbf{c}_j^{\mathrm{H}}, \tag{11}$$

where $L$ represents the number of transmissions, and $c_j$ indicates the compressed signal transmitted during the $j$-th transmission with different subbands. The method is generally employed in complex environments, particularly those with a high number of scatterers, and necessitates over 10 transmissions with varying center frequencies, which can make the transmission and reception times too long to be applicable in real time. To prevent multiple transmissions, in this study, as with filtered FPWC-MVDR, we send the complete bandwidth signal only once. We compress the received signal and divide it into numerous subbands using band-pass filters [39]. The calculation for $\hat{\mathbf{R}}$ is also in Eq. 11, where $L$ represents the number of subbands and $\mathbf{c}_j$ refers to the $j$-th wide subband. Note that varying the center frequency of the subbands widely and finely is crucial for preventing degeneracy of the eigenvalues. Additionally, a wide subband width is necessary for preserving temporal localization.

### C. OUTLINE OF SCM-WEIGHTED SA

When employing SCM for plane wave coherent imaging, multiple FM chirp subband echoes are acquired with varying center frequencies for each transmission angle. The delay profile of SCM is calculated for each transducer element

and then multiplied by the original $c(t)$ in Eq. 5 using an apodization function.

$$x_{kj}(t) = S_k(t)c_{kj}(t), \quad k = 1, 2, \ldots, N, \\ j = 1, 2, \ldots, L, \tag{12}$$

where $N$ is the number of elements, $L$ is the number of subbands, $c_{kj}(t)$ is the compressed signal, and $x_{kj}(t)$ is the compressed signal with SCM weights corresponding to $c_{kj}(t)$. Subsequently, applying time delay of $\tau$ and associated IQ phase correction of $\omega\tau$ for each pixel position, the following two-dimensional matrix can be obtained from $\{x_{kj}(t)\}$.

$$\mathbf{X} = \begin{bmatrix} x_{1,1} & x_{1,2} & \cdots & x_{1,N} \\ x_{2,1} & x_{2,2} & \cdots & x_{2,N} \\ \vdots & \vdots & \ddots & \vdots \\ x_{L,1} & x_{L,2} & \cdots & x_{L,N} \end{bmatrix}. \tag{13}$$

For each transmission that conducts synthetic aperture, the complex brightness value at each pixel location is determined by averaging the element with respect to each subband as follows:

$$y_j = \frac{1}{N}\sum_{k=1}^{N} x_{kj}. \tag{14}$$

The procedure lacks specific definitions for processing transmission angles and subbands, and the commonly used approach involves simple averaging. This study introduces the FPWC-MVDR concept to improve this procedure.

### D. OUTLINE 0F FPWC-MVDR

This subsection presents an overview of FPWC-MVDR, a combination of A-SBC and MV compounding techniques for transmission angles. To enhance comprehension of FPWC-MVDR, we firstly explain DCR-MVDR [29]. For the transmission, DCR-MCDR utilizes plane waves with varying angles [40]. A two-dimensional matrix is obtained as follows:

$$\mathbf{X} = \begin{bmatrix} x_{1,1} & x_{1,2} & \cdots & x_{1,N} \\ x_{2,1} & x_{2,2} & \cdots & x_{2,N} \\ \vdots & \vdots & \ddots & \vdots \\ x_{M,1} & x_{M,2} & \cdots & x_{M,N} \end{bmatrix}, \tag{15}$$

where, unlike Eq. 13, $M$ represents the number of transmission angles. In angle compounding, the angle weights are computed using the MVDR method and the components of $\mathbf{X}$ are added horizontally first, then vertically for element compounding. The brightness value of each pixel represents its magnitude.

Inspired by DCR-MCDR, we proposed FPWC-MVDR by adding A-SBC to DCR-MVDR. The full effective bandwidth of the FM chirp signal is transmitted at each angle. The band-pass filter extracts subbands of various frequencies from the signal acquired in each direction, leading to the formation of a third-order tensor containing the subband direction, the angle direction, and the element direction. Subband compounding also employs frequency weights with MVDR.

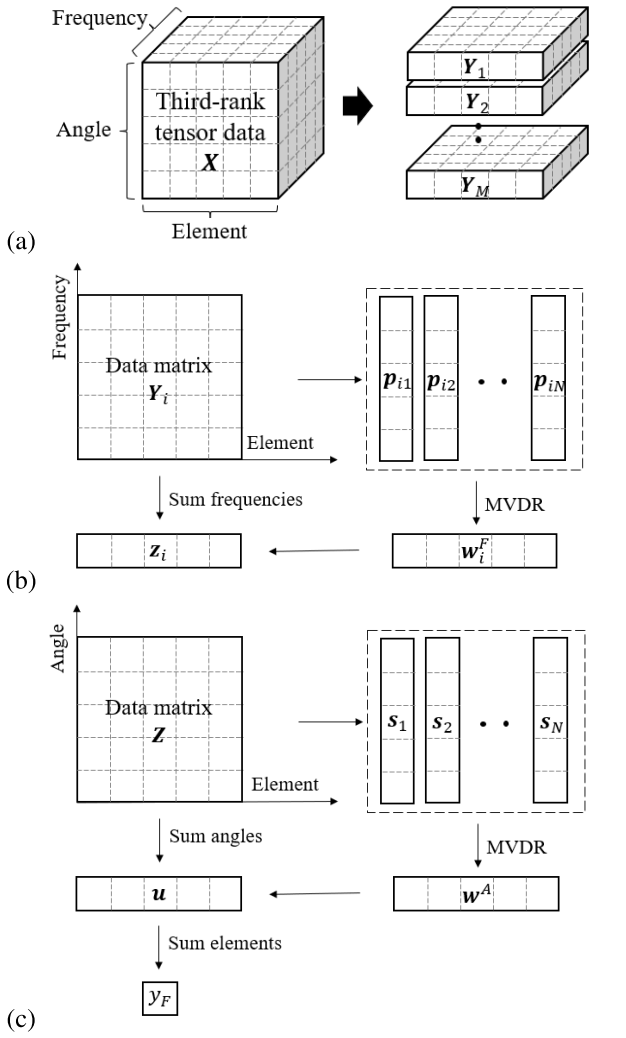


**FIGURE 4.** FPWC-MVDR processing overview: (a) decomposition of the 3rd order tensor data; (b) frequency weights calculation and compound processes; (c) angle compound and FPWC-MVDR output using DAS in the element compound.

After subband compounding, DCR-MVDR is applied to the two-dimensional matrix in the angle and element direction to calculate brightness values for the pixel positions.

### E. INTEGRATION OF SCM AND FPWC-MVDR

The R-MUSIC delay profile is a time-series waveform with positive values. As a result, when R-MUSIC is applied to synthetic aperture and coherence imaging, the profile signal of each element is used directly for RBF without causing positive and negative cancellations in the addition, which leads to excessive interference. Thus, in each transfer, RBF is proposed as SCM-weighted SA using the delay profile from SCM as an apodization. The study showed that while the range resolution was improved, the images obtained for each sub-band had different image quality [26]. Therefore, using the subband average as the final image is not suitable. It does not improve the lateral resolution because it does not properly

compound for different transmissions. In SCM-weighted SA-SCM, the process involves calculating the image for each subband obtained by SCM-weighted SA. Then, SCM calculation is performed for each line in its range direction using the subband information, and a group of subband images are combined into a single image [27]. However, this method has the disadvantage of not improving the resolution in the lateral direction and has a high computational cost due to the double application of SCM.

R-MUSIC is a technique that detects the location of a few reflective scatterers with super-resolution. By processing small regions as a whole, TR-MUSIC [4] can produce an image of multiple scatterers. Although a similar method can be applied to R-MUSIC, a different approach is used in this research. The delay profile of SCM can be calculated for each angle when plane waves are transmitted at different angles. Since scatterers typically exhibit anisotropic reflection properties, delay profiles for different transmission angles are likely to contain different information about the scatterer position. Therefore, by applying the delay profile acquired for each transmission angle to the corresponding received echo, super-resolution of echoes from numerous scatterers can be achieved. The use of FPWC-MVDR on these super-resolution echoes is expected to improve resolution in both the range and lateral directions.

As previously discussed, the combination of SCM and FPWC-MVDR through sub-band extraction improves the resolution in both range and lateral directions, even in the presence of multiple scatterers. The following section details the integration of R-MUSIC, specifically SCM, into the MVDR-based A-SBC, i.e., FPWC-MVDR.

First, the received signals from each transmit angle are compressed, and then multiple subbands with different center frequencies are extracted. These subband signals are then converted to baseband IQ signals and labeled as $i = 1, \cdots, M$ for the transmit angle, $j = 1, \cdots, L$ for the subbands, and $k = 1, \cdots, N$ for the transducer elements. After these steps, the following procedures are performed.

In step 1, the SCM delay profiles $S_{ik}(t)$ for the $k$-th element of the $i$-th angle are calculated using the apodization weights, and then the subbands with the SCM weights $x_{ijk}(t)$ can be derived using the following equation.

$$x_{ijk}(t) = S_{ik}(t)c_{ijk}(t), \quad i = 1, 2, \ldots, M, \\ j = 1, 2, \ldots, L, k = 1, 2, \ldots, N, \tag{16}$$

where $c_{ijk}(t)$ is the original subband IQ signal.

In Step 2, the pixel of interest on the image can be used to obtain $x_{ijk}$ through the application of time delaying and phase correction, from $x_{ijk}(t)$.

In Step 3, the third-order tensor data $X = [x_{ijk}]$ are decomposed into a frequency-array matrix $Y_i = [y_{jk}]$ for each transmission angle (Fig. 4(a)). Subsequently, the frequency components are contracted for each transmission angle (Fig. 4(b)). The formula for the variance covariance in the frequency direction $R_{Fi}$ is as follows:

$$\hat{\mathbf{R}}_{Fi} = \frac{1}{N}\sum_{k=1}^{N} \mathbf{p}_{ik}\mathbf{p}_{ik}^{H} + \epsilon\mathbf{I}, \quad i = 1, 2, \cdots, M, \tag{17}$$

where $\epsilon$ is the diagonal loading parameter related to $\Delta = \mathrm{Tr}(\hat{\mathbf{R}})/\mathrm{Rank}(\hat{\mathbf{R}})$ and $\hat{\mathbf{R}}$ denotes the first term on the right-hand side of Eq. 17. Adjusting the value of $\epsilon$ enhances the robustness of the matrix, and $\mathbf{I}$ is an identity matrix. In Eq. 17, the snapshot vector $\mathbf{p}_{ik}$ is computed as shown below:

$$(\mathbf{p}_{ik})_j = \frac{1}{N-1}\sum_{l=1, l\neq k}^{N} x_{ijl}, \quad i = 1, 2, \cdots, M, \\ k = 1, 2, \cdots, N, j = 1, 2, \cdots, L. \tag{18}$$

Subband weights $\mathbf{w}_i^F$ can be defined by the minimum variance criterion as follows:

$$\mathbf{w}_i^F = \frac{\hat{\mathbf{R}}_{Fi}^{-1}\mathbf{1}_L}{\mathbf{1}_L^{\top}\hat{\mathbf{R}}_{Fi}^{-1}\mathbf{1}_L}, \mathbf{1}_L = [1, \cdots, 1]^{\top}, i = 1, 2, \cdots, M. \tag{19}$$

For the $i$-th angle, the subband compound is given by the following equation:

$$z_{ik} = \sum_{j=1}^{L} (\mathbf{w}_i^F)_j x_{ijk}, i = 1, 2, \cdots, M, k = 1, 2, \cdots, N. \tag{20}$$

In Step 4, similar to the subband compound, the angle compound is as follows:

$$u_k = \sum_{i=1}^{M} \mathbf{w}_i^A z_{ik}, \quad k = 1, 2, \cdots, N, \tag{21}$$

where the angular weights $\mathbf{w}_i^A$ are also calculated using MVDR in the same manner as the subband weights (Fig. 4(c)).

Finally, the elements are combined using DAS to sum the values of all elements. The FPWC-MVDR output for each pixel with SCM weighting process is defined as follows:

$$y_F = \sum_{k=1}^{N} u_k. \tag{22}$$

### F. COHERENCE FACTOR RBF

CF coefficient evaluates the focusing quality of RBF by estimating the ratio of the sum of coherent and incoherent elemental echo signals. When dealing with a set of elemental echo signals with significant focusing errors, CF coefficient becomes significantly low [41]. In this paper, we use the values of each element in Eq. 21 with subband and angle weights to calculate $\hat{w}_{CF}$ as follows:

$$\hat{w}_{CF} = \frac{\left|\frac{1}{N}\sum_{k=1}^{N} u_k\right|^2}{\frac{1}{N}\sum_{k=1}^{N} |u_k|^2} = \frac{\left|\sum_{k=1}^{N} u_k\right|^2}{N\sum_{k=1}^{N} |u_k|^2}. \tag{23}$$

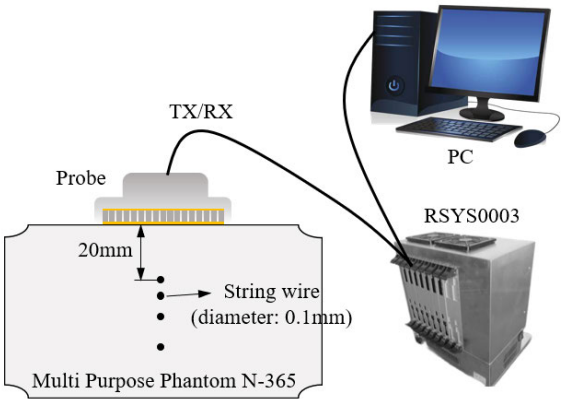


**FIGURE 5.** Experimental settings for the soft tissue-mimicking phantom.

The CF imaging output, denoted as $y_{CF}$ and based on FPWC-MVDR with SCM weight, can be expressed as follows:

$$y_{CF} = \hat{w}_{CF} \cdot \sum_{k=1}^{N} u_k. \tag{24}$$

Compounding using CF coefficients may serve as an alternative to MV compounding for subband and angle compounding. However, evaluating their characteristics and effectiveness is beyond the scope of this paper and will be investigated in future studies.

## III. EXPERIMENTS AND DISCUSSION

### A. EXPERIMENTAL CONDITIONS

During the experiments, we utilized an experimental platform for medical ultrasound applications (RSYS0003, Microsonic Co, Ltd., Japan) to perform the transmit and receive sequences. The sampling frequency was 31.25 MHz and the maximum number of samples was 9473. For the ultrasound transducer, we used a linear array probe (T0-1599, Nihon Dempa Kogyo Co, Ltd., Japan) with a center frequency of 7.5 MHz and specific bandwidth of 70%. A 64-element ultrasonic transducer was used to transmit and receive FM chirp signals. The elements are 0.2 mm thick and the spacing between two elements is 0.115 mm. After receiving all signals, signal processing and beamforming procedures were carried out exclusively in MATLAB R2022b (The MathWorks, Inc., MA, USA).

Fig. 5 displays a diagram of the experimental arrangement. Signals are sent and received within a phantom designed to simulate soft tissue (US-2 Ultrasound quality assurance phantoms N-365, Kyoto Kagaku Co, Ltd., Japan), where the speed of sound is 1432 m/s and the attenuation is 0.59 dB/cm/MHz at a room temperature of 25 °C. In the ultrasonic detection range, there are four string wires arranged in a straight line pattern at the centerline of the probe. The wire closest to the probe is located 20 mm away, with intervals of 1 mm, 2 mm, and 3 mm between the remaining wires. Fig. 6(a) and (b) show the transmitted signal

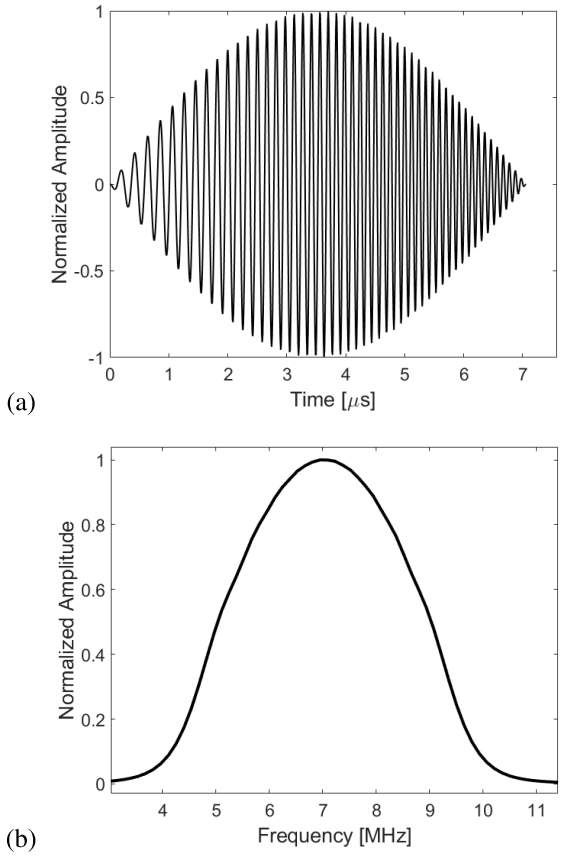


**FIGURE 6.** FM-chirp transmission signal with Hanning window function in (a) the time domain and (b) the frequency domain.

**TABLE 1.** Experimental parameters and values.

| Parameter | Value |
|---|---|
| Transmission method | Plane Wave |
| Transmission voltage | 60 V |
| Transmission angle | From $-8°$ to $8°$ |
| Number of transmission angles | 33 |
| Number of subbands | 12 |
| Subbands freq. | Randomly selected between 4 and 8 MHz |
| Subband bandwidth | 2 MHz |

using a Hanning window function in the time and frequency domains during the experiment. Details of the parameters used in the proposed method can be found in Table 1.

### B. EFFECTIVENESS OF SCM USING FILTERS

After extracting the subbands from the compressed received signal and transforming the real signal to the analytic signal (IQ signal), the eigenvalues of the matrix $\mathbf{R}$ are obtained from Eq. 9 when performing SCM calculation. Fig. 7 shows the eigenvalues ranked from largest to smallest. For this particular experiment, four targets are positioned within the ultrasonic detection region, which defines $D = 4$ in Eq. 10 to distinguish the signal subspace from the noise subspace.

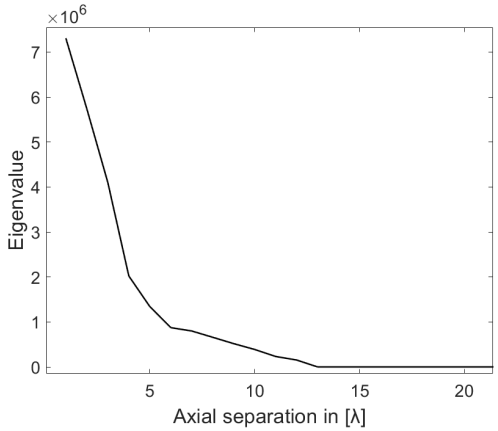


**FIGURE 7.** Plot of eigenvalues of R using Eq. 9.

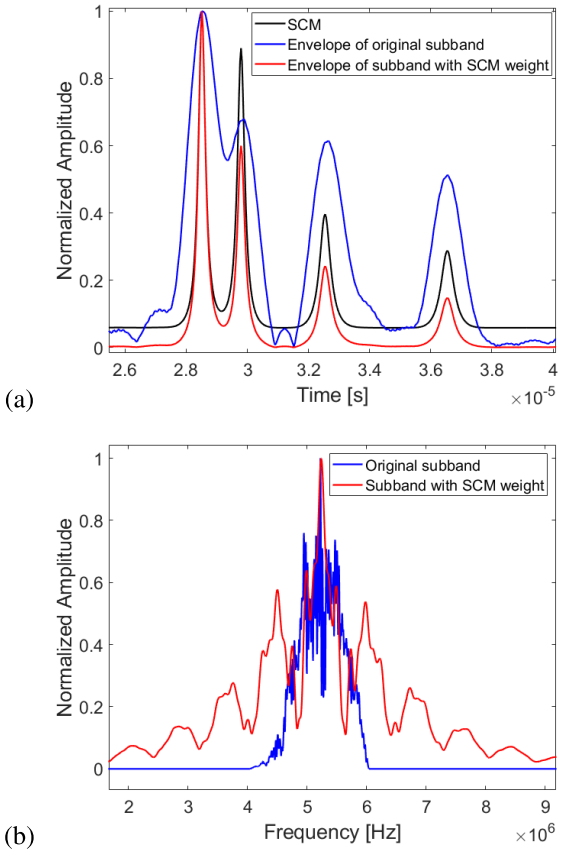


**FIGURE 8.** Comparison of the original received signal and received signal with SCM weights in the (a) time domain and (b) frequency domain.

In this study, the steering vector $\mathbf{r}_i$ is used as an FM chirp signal with a center frequency of 6.68 MHz and a bandwidth of 2 MHz, representing 1 of the 12 extracted subbands. Fig. 8 compares an original subband (without weights) and the same subband with SCM weights calculated according to Eq. 16. In the time domain [see Fig. 8(a)], it is obvious that the original subbands at the two targets are difficult to separate even at a distance of only 0.1 mm. The results obtained by SCM are obviously narrower than those of the original subbands. Furthermore, the subbands with SCM weights are even narrower, and the two target positions are clearly visible. In addition, SCM effectively suppresses the noise amplitude in non-target areas. More interestingly, Fig. 8(b) shows in the frequency domain that the original subband always has a bandwidth of 2 MHz due to the bandpass filter. However, after multiplying SCM weights, the subband waveform changes and has a much wider bandwidth than 2 MHz. Since the bandwidth widens and the axial resolution increases, it can be assumed that the use of SCM weights can further improve the axial resolution.

### C. COMPARISON OF RBFs

To illustrate the effectiveness of our proposed method, we made a comparison with other methods. The B-mode image of CPWC is shown in Fig. 9(a). In the CPWC processing, plane waves are transmitted and received several times at different angles. After applying time delay and phase corrections for each pixel position, the same matrix as in Eq. 15 is obtained. The CPWC output is then determined by averaging the matrix elements as follows:

$$y_{CPWC} = \frac{1}{MN} \sum_{i=1}^{M} \sum_{k=1}^{N} x_{ik}. \tag{25}$$

Fig. 9 shows the B-mode images of the different RBFs. Table 2 outlines the differences between them. Fig. 9(b) shows the B-mode of the CPWC with CF weight, which uses CF beamforming in the element compound. Fig. 9(c) shows the B-mode of the CPWC with SCM weight. Fig. 9(d) shows the B-mode of the FPWC-MVDR method. Fig. 9(e) shows the B-mode of FPWC-MVDR with CF weight in the element compound. Fig. 9(f) shows the B-mode of FPWC-MVDR with SCM weight, while Fig. 9(g) shows the B-mode of FPWC-MVDR using both SCM and CF weight (proposed method).

Comparing Fig. 9(a) and Fig. 9(c), even without using the frequency and angle weights, SCM weights improve the axial resolution, especially at 20 mm and 21 mm, where the two targets can be clearly distinguished. Furthermore, comparing Fig. 9(d) and Fig. 9(f), it can be confirmed that SCM weights applied in the FPWC-MVDR can further improve the axial resolution significantly. The proposed method has the highest axial resolution and almost the same lateral resolution as FPWC-MVDR-CF because the CF weight calculation filters out unwanted signals [see Fig. 9(g)]. In addition, the intensity of background noise is suppressed.

In the intensity distribution profile of the four targets along the axial direction [see Fig. 10(a)], the use of SCM weights can effectively suppress the generation of artifacts outside the target position. However, SCM weights also result in some intensity degradation for three of the targets, except for the target closest to the probe. Fig. 10(b) shows the intensity distribution profile on the lateral line through the

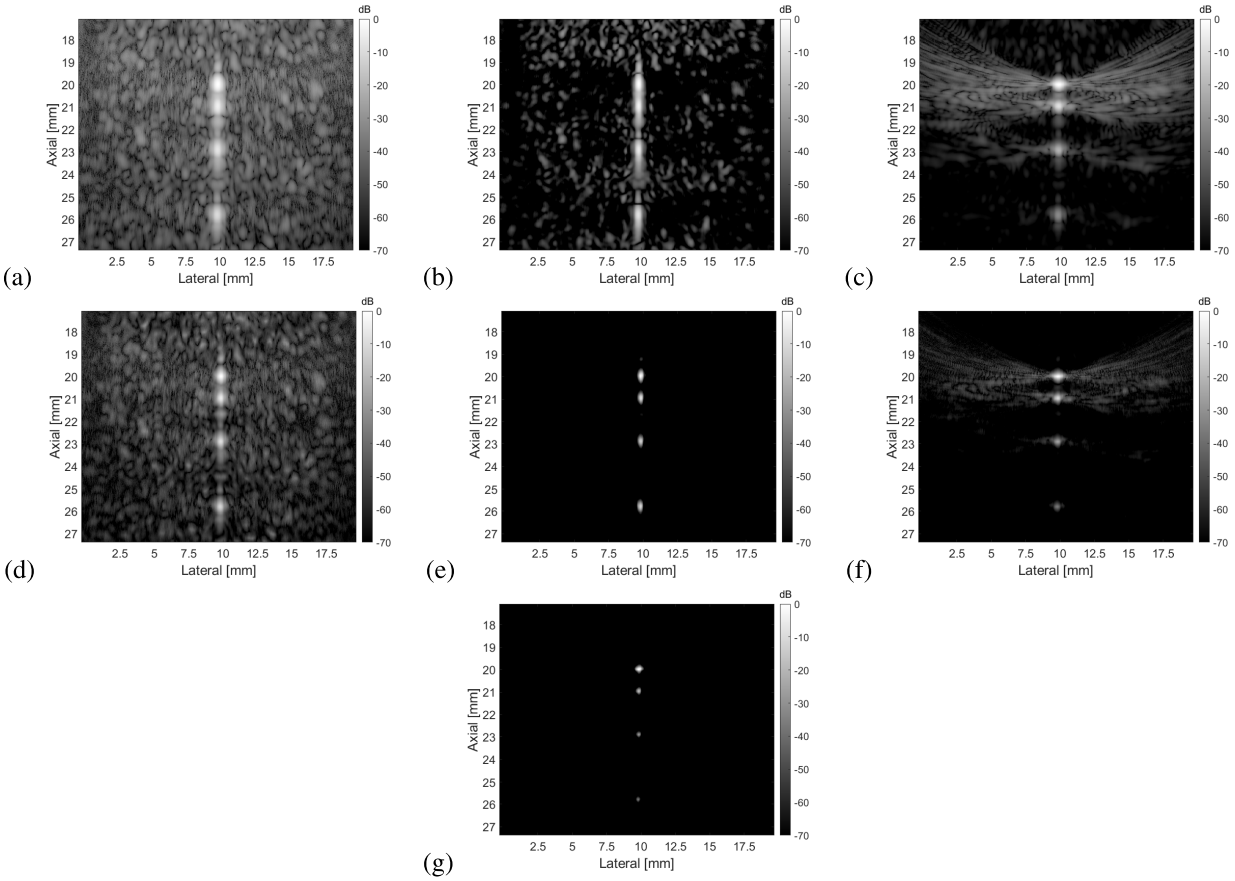


**FIGURE 9.** B-mode image of the (a) CPWC method; (b) CPWC-CF; (c) SCM-CPWC; (d) FPWC-MVDR; (e) FPWC-MVDR-CF; (f) SCM-FPWC-MVDR and (g) SCM-FPWC-MVDR-CF (proposed method).

**TABLE 2.** Differences between RBFs.

| Method | Apodization | Frequency compound | Angle compound | Element compound |
|---|---|---|---|---|
| CPWC | None | Simply adding | Simply adding | Simply adding |
| CPWC-CF | None | Simply adding | Simply adding | CF |
| SCM-CPWC | SCM | Simply adding | Simply adding | Simply adding |
| FPWC-MVDR | None | MVDR | MVDR | Simply adding |
| FPWC-MVDR-CF | None | MVDR | MVDR | CF |
| SCM-FPWC-MVDR | SCM | MVDR | MVDR | Simply adding |
| SCM-FPWC-MVDR-CF (Proposed method) | SCM | MVDR | MVDR | CF |

foremost target, confirming that the use of CF weights in the element compound can effectively reduce the sidelobe level. In addition, the analysis of the B-mode image in SCM-FPWC-MVDR shows that the sidelobe level at 20 mm in the axial direction is higher than in other areas [see Fig. 9(f)], but Fig. 10(b) shows that the sidelobe level at 20 mm is still lower than that of FPWC-MVDR. As shown in Fig. 10, the proposed method has the best resolution and greatly suppresses the generation of artifacts in the axial direction.

Fig. 11 shows the mean half-maximum full width of the four targets for each method, calculated using the −6 dB pulse widths shown in Fig. 10(a) and (b). The implementation of CF weights on the element compound resulted in a significant improvement in lateral resolution. Although SCM weights were not successful in improving the lateral resolution, there was a significant improvement in the axial resolution.

Fig. 12 shows the speckle level, which is defined as the average level of speckle intensity relative to the signal level. Excluding the rectangular area measuring 18.5 mm to 26.5 mm in the range direction and 8 mm to 12 mm in the lateral direction, the average level of the area is based on the B-mode image. The proposed method shows a noticeable reduction in speckle level as a result of implementing SCM

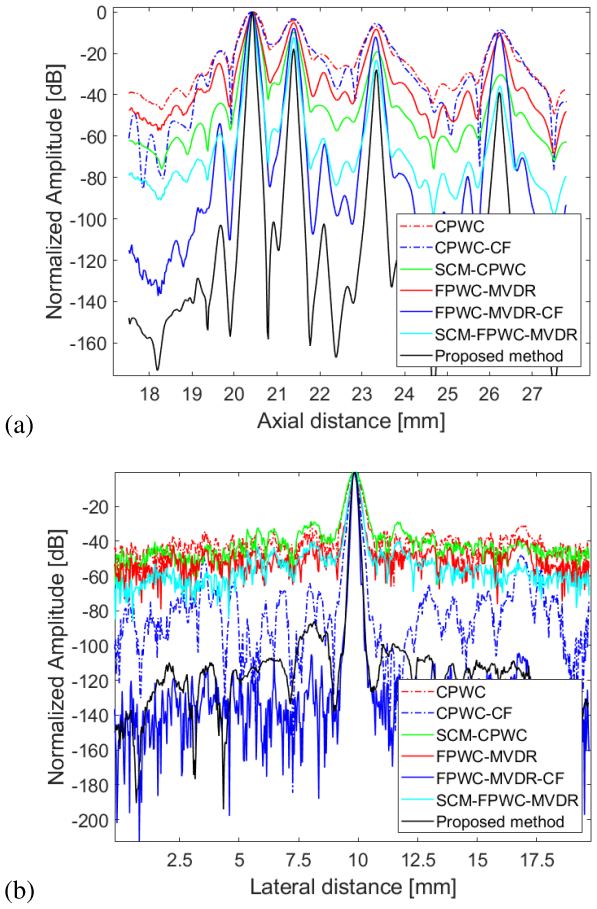


**FIGURE 10.** Intensity distribution profile comparison on the (a) axial line at the center of the B-mode image and (b) the lateral line through the foremost target.

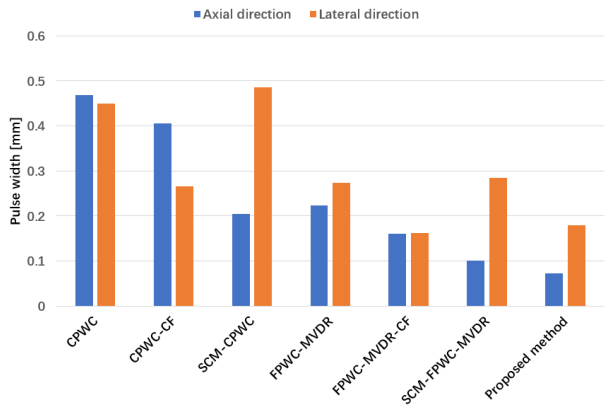


**FIGURE 11.** Resolution comparison in the axial and lateral direction.

weighting, CF weighting and MVDR in both frequency and angular directions to suppress noise intensity.

### D. CHARACTERIZATION OF THE NUMBER OF SIGNAL AND NOISE SUBSPACE EIGENVALUES

Unlike the experiment, the reality of ultrasound diagnosis is complicated, it is impractical to accurately determine the

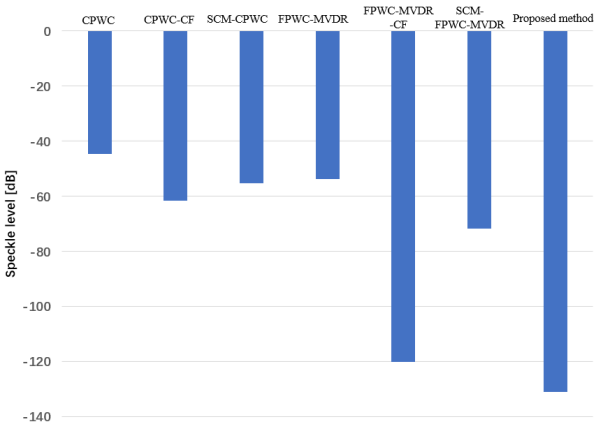


**FIGURE 12.** Speckle level comparison.

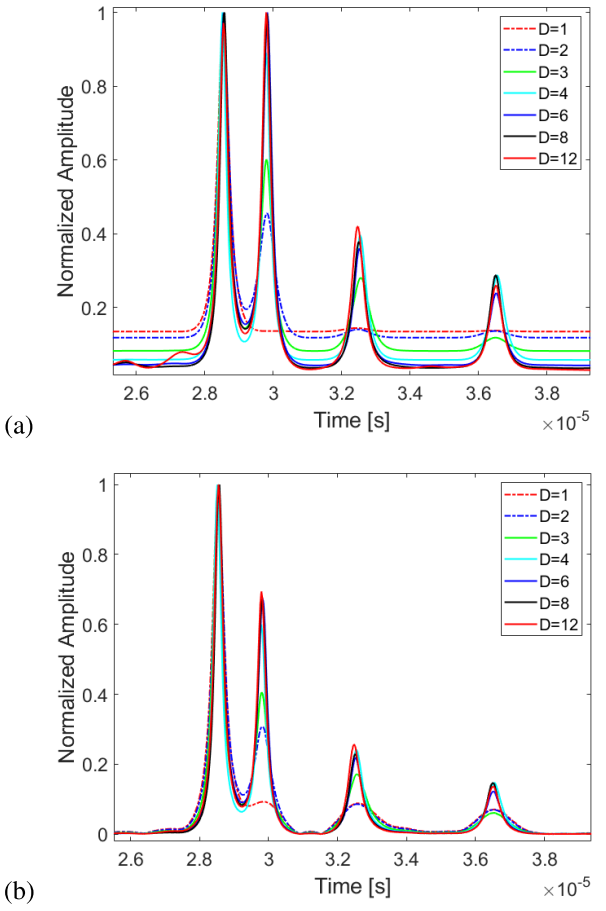


**FIGURE 13.** When $D$ has different values in Eq. 10, (a) the result of the SCM corresponds to (b) the envelope of the subband with SCM weights.

number of targets within the ultrasound scan area before imaging. In this section, we examine the relationship between the number of signal subspace eigenvalues $D$ from Eq. 10 and the number of real targets $Q$. When $D \geq Q$, all $Q$ targets in the ultrasound scan region can be displayed, the resolution and

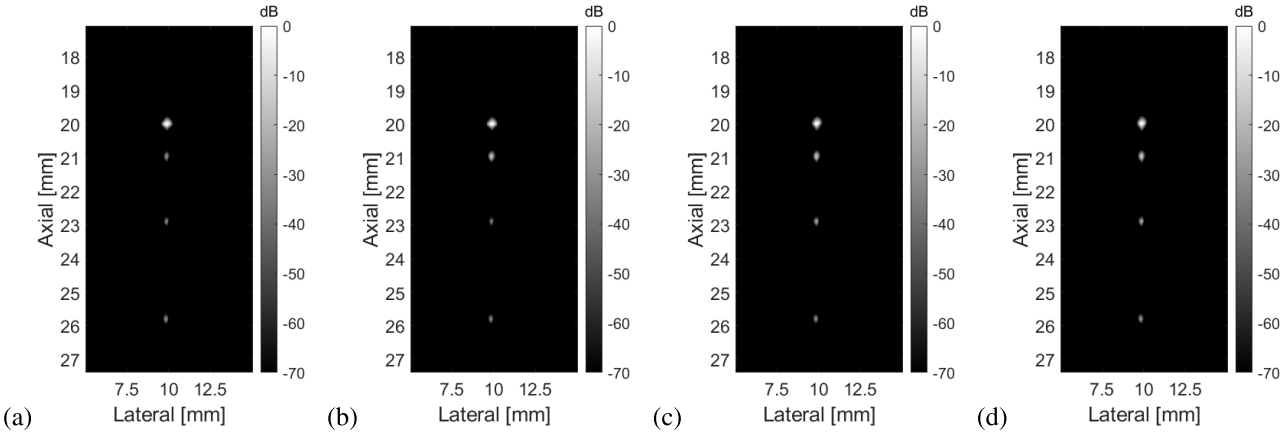


**FIGURE 14.** Changes in B-mode images obtained using the proposed method with different values of $D$ from Eq. 10. The values of $D$ are (a) 1; (b) 2; (c) 8 and (d) 12.

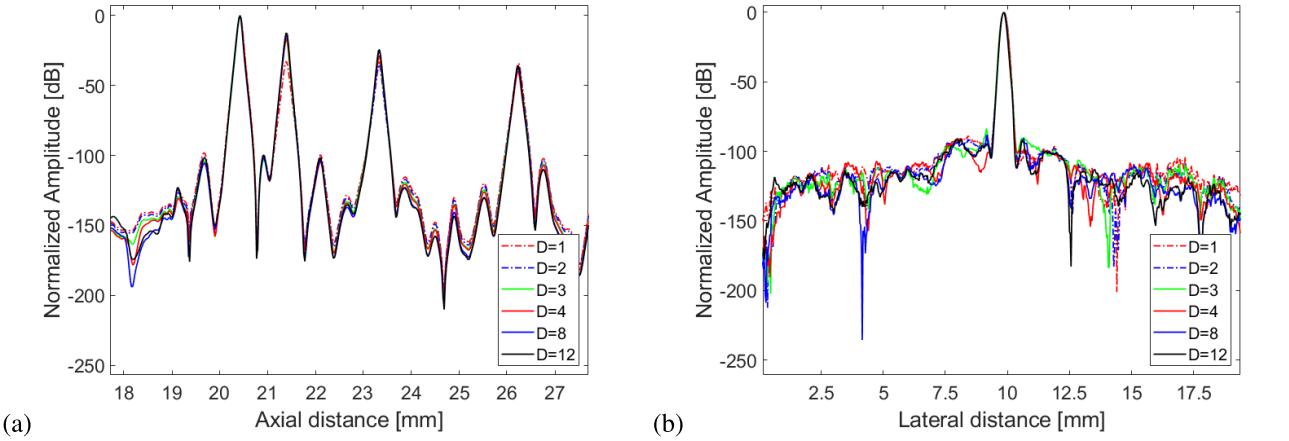


**FIGURE 15.** Intensity distribution profiles from the proposed method with different values of $D$ on the (a) axial line at the center of the B-mode image and (b) the lateral line through the foremost target.

speckle level are approximately the same as when $D = Q$. Experiments have been performed to verify this hypothesis.

The experimental conditions were the same as in Sect. III-A, with the actual number of targets in the ultrasonic scan range $Q = 4$ and $L = 12$ subbands. Fig. 13(a) shows the results of SCM when $D$ has different values. When $1 \leq D < Q$, the SCM peaks at the probe positions closest to the $D$ target; however, the value of SCM from the $D+1$-th to the $Q$-th target positions tends to be close to, but not equal to, 0. When $Q \leq D \leq L$, the peaks appear at all $Q$ target positions. The intensity of the peaks does not change significantly with the change in $D$. The envelope of the subband with SCM weights using different values of $D$ is shown in Fig. 13(b). When $1 \leq D < Q$, the signal intensity of $D$ target positions closest to the probe is strong and weak from $D+1$ to $Q$ target positions; however, their positions are still observed. When $Q \leq D \leq L$, the signal intensities at all $Q$ target positions are strong.

Fig. 14 shows a part of the B-mode images using the proposed method when $D$ has different values. Fig. 15(a) shows the intensity distribution profiles from the proposed method on the axial line at the center of the B-mode image, and Fig. 15(b) shows profiles on the lateral line through the foremost target. The intensity at each target position is essentially stable as the value of $D$ varies when $Q \leq D \leq L$. The pulse width and speckle level are also essentially the same. Furthermore, when $1 \leq D < Q$, the proposed method still shows the target positions clearly. However, the intensity of the target position is less than that in $Q \leq D \leq L$. In this experiment, the average intensity at the target positions is 18 dB less when $D = 1$ than when $D \geq 4$, and 9 dB less when $D = 2$ than when $D \geq 4$.

### E. IN VIVO STUDY: HUMAN CAROTID ARTERIES

Due to the complicated composition of biological tissues, *in-vivo* imaging is essential to verify the proposed method. The parameters and values for the carotid artery experiment are elaborated in Table 3. To account for the presence of more scatterers in the human environment, the number of extracted subbands was increased to 54 and $D$ in Eq. 10 for

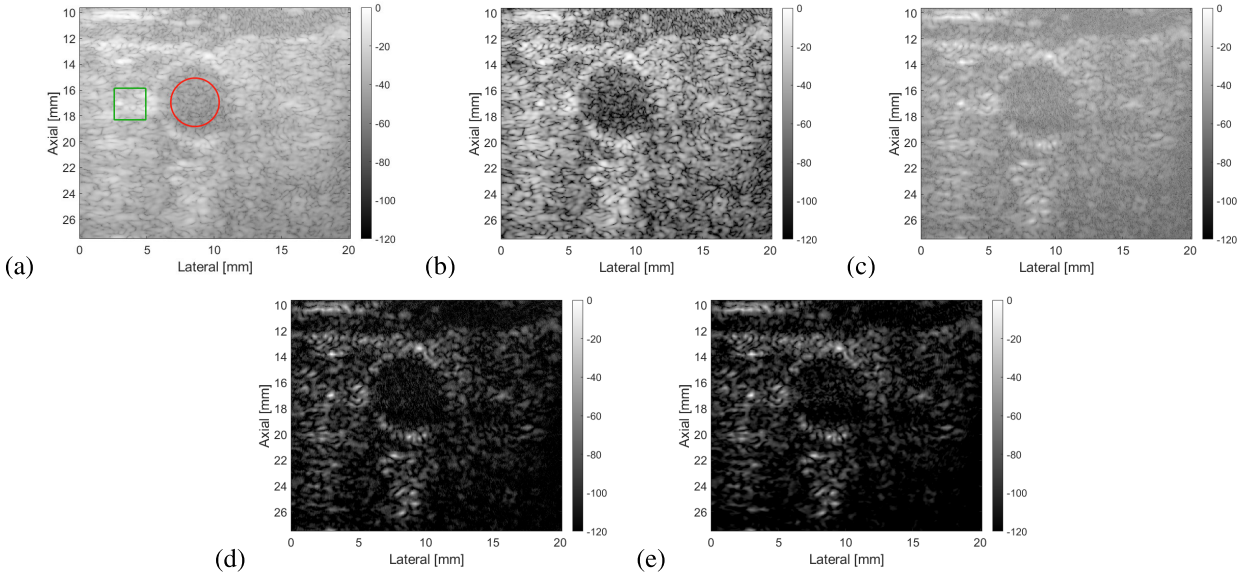


**FIGURE 16.** *In-vivo* transverse cross images of the carotid artery using different methods: (a) CPWC method; (b) CPWC-CF; (c) FPWC-MVDR; (d) FPWC-MVDR-CF and (e) SCM-FPWC-MVDR-CF weight (proposed method).

**TABLE 3.** Parameters and values for the carotid artery experiment.

| Parameter | Value |
|---|---|
| Transmission angle | From $-8°$ to $8°$ |
| Number of transmission angles | 33 |
| Number of subbands | 54 |
| Subbands freq. | Randomly selected between 4 and 8 MHz |
| Subband bandwidth | 2 MHz |
| Number of $D$ from Eq. 10 | 30 |

**TABLE 4.** CR, CNR and sSNR of the carotid artery images for different methods.

| Method | CR(dB) | CNR | sSNR |
|---|---|---|---|
| CPWC | 27.30 | 2.67 | 2.42 |
| CPWC-CF | 52.52 | 2.01 | 1.63 |
| FPWC-MVDR | 24.27 | 2.06 | 2.74 |
| FPWC-MVDR-CF | 49.26 | 1.70 | 2.82 |
| Proposed method | 51.18 | 1.75 | 2.91 |

calculating SCM was increased to 30 for effective scatterer detection. Fig. 16 shows the images of a human carotid artery obtained by different methods. For a more accurate comparison, we performed quantitative evaluations of *in-vivo* images using image quality metrics. Specifically, we define the contrast ratio CR $= u_b - u_c$, contrast-to-noise ratio CNR $= |u_b - u_c|/\sqrt{\sigma_b^2 + \sigma_c^2}$, and speckle signal-to-noise ratio sSNR $= u_b/\sigma_b$, using the average speckle intensity (the green rectangle area in Fig. 16(a)) $u_b$, the average intensity amplitude of the carotid artery area (the red circle area in Fig. 16(a)) $u_c$, and their standard deviations $\sigma_b$ and $\sigma_c$, respectively.

Table 4 shows a comparison of CR, CNR and sSNR. To verify the resolution of the different methods, we also calculated the autocorrelation functions of the B-mode images in the axial and lateral directions for the different methods [see Fig. 17(a) and (b)]. The autocorrelation function yields the power spectrum after Fourier transform, making it a valuable tool for assessing the frequency distribution of irregular signals. Our study uses the autocorrelation function under the assumption that high resolution within the speckle domain indicates the presence of significant high frequency components. This assumption is based on the irregular nature of speckle patterns, where visualization at high resolution is expected to facilitate the visualization of point scatterers.

The results show that CPWC-CF, FPWC-MVDR-CF, and the proposed method achieve high CR performance by using CF weights, but at the expense of reduced CNR performance. FPWC-MVDR, FPWC-MVDR-CF and the proposed method exhibit high sSNR performance due to the noise intensity suppression effect of MVDR. In addition, the proposed method not only provides high CR, but also achieves the highest sSNR by using SCM weights. Furthermore, as shown in Fig. 17, the proposed method exhibits slightly higher axial and lateral resolution compared to FPWC-MVDR-CF and significantly outperforms other methods.

### F. SIMULATION USING MILLIMETER WAVES

With the emergence and utilization of 5G technology, millimeter wave research has come to the forefront. Considering the high frequency and large bandwidth of millimeter wave, our proposed method has the potential to provide super-resolution in the wideband case [42]. Therefore, we use MATLAB software to simulate the influence of SCM on high frequencies under ideal conditions.

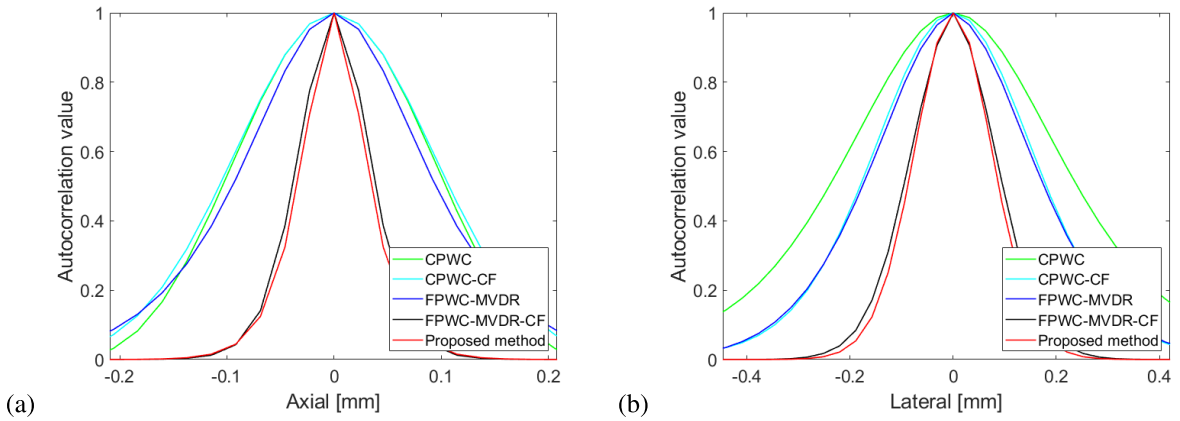


**FIGURE 17.** Autocorrelation function from the B-mode images of the carotid artery using different methods in (a) the axial direction and (b) the lateral direction.

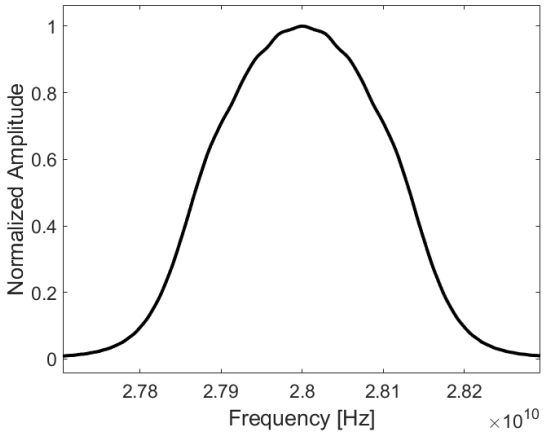


**FIGURE 18.** Spectral amplitude distribution of the transmission using Hanning window function in the millimeter-wave simulation.

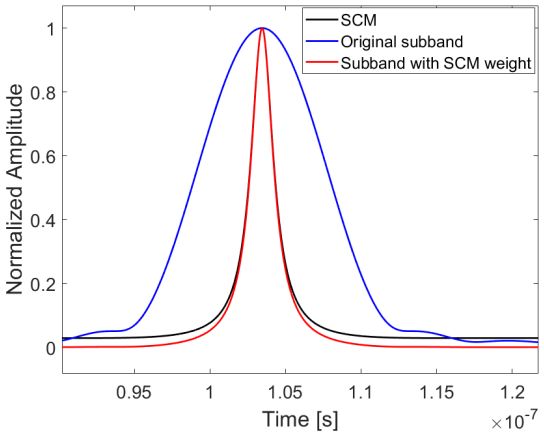


**FIGURE 19.** Comparison of the original received signal and received signal with SCM weights in the time domain of the millimeter-wave simulation.

The simulation uses an FM chirp signal with a center frequency of 28 GHz and a bandwidth of 400 MHz as the transmit signal [see Fig. 18]. The propagation velocity is $3 \times 10^8$ m/s. There are 16 array antenna units with a unit pitch of 0.2mm. The array antenna transmits 7 times at 2 degree intervals between $-6$ degree and $+6$ degree with plane wave. A single point target is positioned 14 m from the array antenna.

In the SCM process, the received signal is randomly extracted by the bandpass filter into 12 subbands with different center frequencies and a bandwidth of 200 MHz. A comparison of the original received signal and the received signal with SCM weights in the time domain is shown in Fig. 19. The results show that the subbands with SCM weights are significantly narrower than the original subbands. For a more detailed comparison, Fig. 20 (a), (b) and (c) show the B-mode images of CPWC-CF, FPWC-MVDR-CF and the proposed method, respectively. In addition, we present Fig. 21(a) and (b) to show the comparison of the intensity distribution profiles in the axial and lateral directions. The axial resolution of the proposed method is significantly improved compared to CPWC-CF and FPWC-MVDR-CF, while the lateral resolution of the proposed method is comparable to FPWC-MVDR with CF weight and slightly better than CPWC with CF weight. In addition, the method effectively suppresses axial sidelobes.

### G. DISCUSSION

The wire-as-target experiment validates the successful extraction of multiple narrow-bandwidth subbands for SCM computation using the full-bandwidth FM chirp signal. The subbands with the SCM weights have narrower pulse widths than the original subbands. Spectral analysis shows that the subbands with SCM weights have significantly wider bandwidths than the original subbands extracted by the bandpass filter. The implementation of SCM in RBF can significantly improve axial resolution, and most targets can be clearly distinguished even at very short distances. SCM

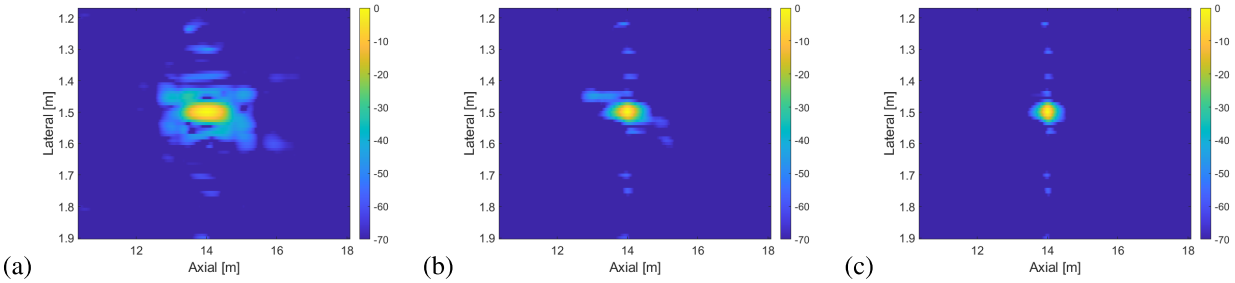


**FIGURE 20.** B-mode image of the (a) CPWC-CF; (b) FPWC-MVDR-CF and (c) SCM-FPWC-MVDR-CF (proposed method) in the millimeter-wave simulation.

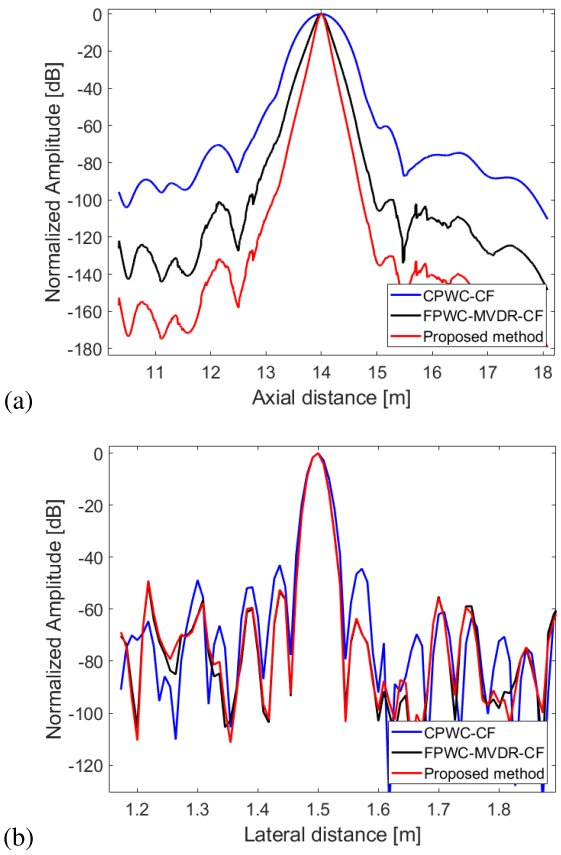


**FIGURE 21.** Intensity distribution profile comparison on the (a) axial line at the center of the B-mode image and (b) the lateral line through the foremost target in the millimeter-wave simulation.

also suppresses noise intensity by distinguishing the signal subspace from the noise subspace, resulting in improved speckle levels.

By quantifying the correlation between the signal subspace eigenvalues and their corresponding number of eigenvectors $D$ [from Eq. 10] and the actual number of targets, all targets can be observed when $D$ is greater than or equal to the actual number of targets and $D$ is less than or equal to the number of subbands. When performing the SCM calculation, it should be noted that the steering vector $\mathbf{r}_i$ from eq. 10 uses signals collected from ideal environments. Since the attenuation and diffraction factors of the signal during actual transmission are not taken into account, there is a reduction in signal intensity at targets that are farther away from each transducer element.

Using CF weights to compute coherence between transducer elements in the element compound results in a significant improvement in lateral resolution. By eliminating unwanted signals at locations away from the target, CF weights reduce the sidelobe level, especially in the lateral direction. The application of SCM further reduces the side lobe at the target in the lateral direction.

FPWC-MVDR uses MVDR to compute the frequency and angle weights because low and high frequencies and each angle are mutually suppressed, resulting in improved axial and lateral resolution and reduced speckle levels. In addition, the application of subbands with SCM weights to FPWC-MVDR significantly improves axial resolution and suppresses background noise. The use of CF weights in the element compound, as opposed to DAS, resulted in a significant improvement in the performance of the proposed method. Its effectiveness is particularly evident in the detection of speckle. Furthermore, our proposed method is applicable not only to ultrasound but also to broadband millimeter waves, as demonstrated by simulations.

Finally, the *in-vivo* carotid artery experiments indicate that increasing the number of subbands and the value of the signal subspace eigenvalues $D$ improves the detection of scattered objects by SCM, which in turn improves the imaging quality. Even when the imaging distance is too large, the proposed method is still viable by calculating the SCM profiles at regular time intervals to maintain proper imaging quality. Although the proposed method has a slight suppression of the tissue background, we believe that it is more suitable for the detection of well-defined structural bodies, such as breast cancer, heart wall, and blood vessels, and that the method allows a clearer observation of the movement of the structural body.

## IV. CONCLUSION

This paper presents a multi-angle transmission using a full-bandwidth FM chirp signal in the form of a plane wave, and the received signal is extracted with a bandpass filter with subbands of different center frequencies for SCM.

FPWC-MVDR is performed using subbands with SCM weights and in the final element combination using CF beamforming instead of the previous DAS. The proposed method was experimentally verified, and the resolution was greatly improved in the axial and lateral directions. The speckle level was also significantly reduced. We also learned that even when the value of $D$ in Eq. 10 was larger than the actual number of targets $Q$, the resolution and speckle level of the proposed method were almost equal to those when $D = Q$. However, when $D < Q$, all the targets were also visible and only the intensity was reduced. The effectiveness of the proposed method was validated by *in-vivo* carotid artery experiments. Furthermore, millimeter-wave simulations showed that the approach is also applicable to optical signals.

Traditionally, the RBF calculations have relied on adaptive weights within a single domain. However, this study introduces a novel approach to improve the performance of RBF by using different adaptive weights in multiple domains, such as frequency, angle, and element, simultaneously.

At present, the main limitations of the proposed method are: (1) This study did not account for signal attenuation and diffraction in SCM calculation, leading to a potential weakening of the signal intensity in situations involving multiple targets. (2) The experiment was conducted with a smaller number of targets than subbands. When the number of targets exceeds the number of subbands, we suggest using a time window. This involves dividing the received signal into multiple segments in the time domain and performing SCM calculations individually. We believe this approach effectively handles the situation.

FDMAS and GCF have shown promising results in improving spatial and contrast resolution while preserving clinical information such as tissue background. In this study, we used CF in the elemental compound. In the future, we will apply FDMAS and GCF in the elemental compound and compare them with the current method. It would be interesting to introduce the concept of TR-MUSIC into the proposed method, or to investigate a method without RBF by synthesizing TR-MUSIC and R-MUSIC.

Finally, the proposed method uses adaptive weight calculations on multiple domains simultaneously, which results in a large computational burden and long running time. To reduce the computational burden and shorten the running time, deep learning is employed with the proposed method [43], [44]. The application of deep learning can improve the performance of RBF, and further efforts can be made to reduce the computational requirements.

## AUTHOR CONTRIBUTIONS

Jie Zheng and Jing Zhu contributed equally to this work: designed the methods, analyzed the data, and wrote the manuscript; Norio Tagawa: initiated and supervised the work.

## DECLARATION OF INTEREST

The authors declare no conflict of interest.

## REFERENCES

[1] T. Misaridis and J. A. Jensen, "Use of modulated excitation signals in medical ultrasound. Part II: Design and performance for medical imaging applications," *IEEE Trans. Ultrason., Ferroelectr. Freq. Control*, vol. 52, no. 2, pp. 192–207, Feb. 2005, doi: 10.1109/TUFFC.2005.1406546.

[2] M. Suzuki, N. Tagawa, M. Yoshizawa, and T. Irie, "Effects of flexural vibration and thickness vibration on receiving characteristics of a diaphragm-type PZT resonator," *Jpn. J. Appl. Phys.*, vol. 59, pp. 1–8, Apr. 2020, Art. no. SKKE10, doi: 10.35848/1347-4065/ab80a0.

[3] M. Oelze, "Bandwidth and resolution enhancement through pulse compression," *IEEE Trans. Ultrason., Ferroelectr., Freq. Control*, vol. 54, no. 4, pp. 768–781, Apr. 2007, doi: 10.1109/TUFFC.2007.310.

[4] Y. Labyed and L. Huang, "Ultrasound time-reversal MUSIC imaging with diffraction and attenuation compensation," *IEEE Trans. Ultrason., Ferroelectr., Freq. Control*, vol. 59, no. 10, pp. 2186–2200, Oct. 2012, doi: 10.1109/TUFFC.2012.2445.

[5] Y. Labyed and L. Huang, "Super-resolution ultrasound imaging using a phase-coherent MUSIC method with compensation for the phase response of transducer elements," *IEEE Trans. Ultrason., Ferroelectr., Freq. Control*, vol. 60, no. 6, pp. 1048–1060, Jun. 2013, doi: 10.1109/TUFFC.2013.2669.

[6] J. Capon, "High-resolution frequency-wavenumber spectrum analysis," *Proc. IEEE*, vol. 57, no. 8, pp. 1408–1418, Aug. 1969, doi: 10.1109/PROC.1969.7278.

[7] F. Prieur, O. M. H. Rindal, and A. Austeng, "Signal coherence and image amplitude with the filtered delay multiply and sum beamformer," *IEEE Trans. Ultrason., Ferroelectr., Freq. Control*, vol. 65, no. 7, pp. 1133–1140, Jul. 2018, doi: 10.1109/TUFFC.2018.2831789.

[8] P.-C. Li and M.-L. Li, "Adaptive imaging using the generalized coherence factor," *IEEE Trans. Ultrason., Ferroelectr., Freq. Control*, vol. 50, no. 2, pp. 128–141, Feb. 2003, doi: 10.1109/TUFFC.2003.1182117.

[9] F. Vignon and M. R. Burcher, "Capon beamforming in medical ultrasound imaging with focused beams," *IEEE Trans. Ultrason., Ferroelectr., Freq. Control*, vol. 55, no. 3, pp. 619–628, Mar. 2008, doi: 10.1109/TUFFC.2008.686.

[10] R. Kozai, K. Okubo, N. Tagawa, T. Irie, and M. Yoshizawa, "Construction of FDMAS in baseband and its performance evaluation," in *Proc. IEEE Int. Ultrasonics Symp*, Glasgow, U.K., Oct. 2019, pp. 320–323, doi: 10.1109/ULTSYM.2019.8925611.

[11] C.-C. Shen, Y.-Q. Xing, and G. Jeng, "Autocorrelation-based generalized coherence factor for low-complexity adaptive beamforming," *Ultrasonics*, vol. 72, pp. 177–183, Dec. 2016, doi: 10.1016/j.ultras.2016.07.015.

[12] T. H. Gan, D. A. Hutchins, D. R. Billson, and D. W. Schindel, "The use of broadband acoustic transducers and pulse-compression techniques for air-coupled ultrasonic imaging," *Ultrasonics*, vol. 39, no. 3, pp. 181–194, Apr. 2001, doi: 10.1016/S0041-624X(00)00059-7.

[13] F. Lam and J. Szilard, "Pulse compression techniques in ultrasonic non-destructive testing," *Ultrasonics*, vol. 14, no. 3, pp. 111–114, May 1976, doi: 10.1016/0041-624X(76)90083-4.

[14] H. Nomura, H. Adachi, and T. Kamakura, "Feasibility of low-frequency ultrasound imaging using pulse compressed parametric ultrasound," *Ultrasonics*, vol. 89, pp. 64–73, Sep. 2018, doi: 10.1016/j.ultras.2018.04.007.

[15] Y. M. Benane, D. Bujoreanu, R. J. Lavarello, F. Varray, J.-M. Escoffre, A. Novell, C. Cachard, and O. Basset, "Experimental implementation of a pulse compression technique using coherent plane-wave compounding," *IEEE Trans. Ultrason., Ferroelectr., Freq. Control*, vol. 65, no. 6, pp. 1025–1036, Jun. 2018, doi: 10.1109/TUFFC.2018.2820747.

[16] M. Tanabe, T. Yamamura, K. Okubo, and N. Tagawa, "Medical ultrasound imaging using pulse compression technique based on split and merge strategy," *Jpn. J. Appl. Phys.*, vol. 49, pp. 1–7, Jul. 2010, Art. no. 07HF15, doi: 10.1143/JJAP.49.07HF15.

[17] M. Fujiwara, K. Okubo, and N. Tagawa, "A novel technique for high resolution ultrasound imaging super resolution FM-chirp correlation method (SCM)," in *Proc. IEEE Int. Ultrason. Symp*, Rome, Italy, Sep. 2009, pp. 2390–2393, doi: 10.1109/ULTSYM.2009.5441857.

[18] N. Tagawa and J. Zhu, "Super-resolution ultrasound imaging based on the phase of the carrier wave without deterioration by grating lobes," in *Proc. 24th Int. Conf. Pattern Recognit. (ICPR)*, Beijing, China, Aug. 2018, pp. 2791–2796, doi: 10.1109/ICPR.2018.8546047.

[19] J. Zheng, N. Tagawa, M. Yoshizawa, and T. Irie, "Subband compound with fundamental wave and harmonics in focus wave beamforming," *Jpn. J. Appl. Phys.*, vol. 61, pp. 1–8, Jun. 2022, Art. no. SG1072, doi: 10.35848/1347-4065/ac5535.

[20] B. M. Asl and A. Mahloojifar, "A low-complexity adaptive beamformer for ultrasound imaging using structured covariance matrix," *IEEE Trans. Ultrason., Ferroelectr., Freq. Control*, vol. 59, no. 4, pp. 660–667, Apr. 2012, doi: 10.1109/TUFFC.2012.2244.
[21] Y. Wang, C. Zheng, H. Peng, and C. Zhang, "Coherent plane-wave compounding based on normalized autocorrelation factor," *IEEE Access*, vol. 6, pp. 36927–36938, 2018, doi: 10.1109/ACCESS.2018.2852641.
[22] J. Zhu and N. Tagawa, "Computationally efficient super resolution ultrasound imaging based on multiple transmission/reception with different carrier frequencies," in *Proc. Meetings Acoust.*, Apr. 2018, vol. 32, no. 1, pp. 1–5, doi: 10.1121/2.0000710.
[23] Y. Asakura, K. Okubo, and N. Tagawa, "Experimental examination of acoustic sensing using super-directivity speaker and super-resolution signal processing with pulse compression technique," *J. Acoust. Soc. Amer.*, vol. 140, no. 4, p. 3274, Oct. 2016, doi: 10.1121/1.4970397.
[24] M. Fujiwara, K. Okubo, and N. Tagawa, "Ultrasound imaging using super resolution FM-chirp correlation method," in *Proc. 30th Symp. Ultrason. Electron.*, Kyoto, Japan, Nov. 2009, pp. 1–2, Paper 3P5-7, doi: 10.24492/use.30.0_537.
[25] T. Wada, Y. Ho, K. Okubo, N. Tagawa, and Y. Hirose, "High frame rate super resolution imaging based on ultrasound synthetic aperture scheme," *Phys. Proc.*, vol. 70, pp. 1216–1220, Jan. 2015, doi: 10.1016/j.phpro.2015.08.262.
[26] J. Zhu and N. Tagawa, "Improvement of performance degradation in synthetic aperture extension of enhanced axial resolution ultrasound imaging based on frequency sweep," *Sensors*, vol. 19, no. 10, p. 2414, May 2019, doi: 10.3390/s19102414.
[27] J. Zhu and N. Tagawa, "High resolution ultrasonic imaging based on frequency sweep in both of transducer element domain and imaging line domain," *Jpn. J. Appl. Phys.*, vol. 58, Jun. 2019, Art. no. SGGE03, doi: 10.7567/1347-4065/ab1000.
[28] R. Kozai, N. Tagawa, M. Yoshizawa, and T. Irie, "Optimization of frequency and plane- wave compounding by minimum variance beamforming," in *Proc. IEEE Int. Ultrasonics Symp*, Las Vegas, NV, USA, Sep. 2020, pp. 1–5, doi: 10.1109/IUS46767.2020.9251727.
[29] N. Q. Nguyen and R. W. Prager, "A spatial coherence approach to minimum variance beamforming for plane-wave compounding," *IEEE Trans. Ultrason., Ferroelectr., Freq. Control*, vol. 65, no. 4, pp. 522–534, Apr. 2018, doi: 10.1109/TUFFC.2018.2793580.
[30] J. Zheng, N. Tagawa, M. Yoshizawa, and T. Irie, "Plane wave beamforming with adaptively weighted frequency compound using bandpass filtering," *Jpn. J. Appl. Phys.*, vol. 60, pp. 1–15, May 2021, Art. no. SDDB08, doi: 10.35848/1347-4065/abf989.
[31] J. Zheng, S. Liu, N. Tagawa, M. Yoshizawa, and T. Irie, "Plane wave beamforming using each frequency with adaptive weight," in *Proc. 41th Symp. Ultrason. Electron.*, Osaka, Japan, Nov. 2020, pp. 1–2, Paper 1J4-2, doi: 10.24492/use.41.0_1J4-2.
[32] J. Zheng, N. Tagawa, M. Yoshizawa, and T. Irie, "Subband compound with harmonics in plane wave beamforming," in *Proc. 42th Symp. Ultrason. Electron.*, Oct. 2021, Paper 2Pb2-5, pp. 1–2, doi: 10.24492/use.42.0_2Pb2-5.
[33] J. Zheng, N. Tagawa, M. Yoshizawa, and T. Irie, "Adaptive realization based on one transmission and reception of simultaneous subband compound of harmonics," in *Proc. IEEE UFFC Latin Amer. Ultrason. Symp. (LAUS)*, Gainesville, FL, USA, Oct. 2021, pp. 1–4, doi: 10.1109/LAUS53676.2021.9639150.
[34] C. C. Nilsen and S. Holm, "Wiener beamforming and the coherence factor in ultrasound imaging," *IEEE Trans. Ultrason., Ferroelectr., Freq. Control*, vol. 57, no. 6, pp. 1329–1346, Jun. 2010, doi: 10.1109/TUFFC.2010.1553.
[35] M. Xu, X. Yang, M. Ding, and M. Yuchi, "Spatio-temporally smoothed coherence factor for ultrasound imaging [correspondence]," *IEEE Trans. Ultrason., Ferroelectr., Freq. Control*, vol. 61, no. 1, pp. 182–190, Jan. 2014, doi: 10.1109/tuffc.2014.6689786.
[36] B. M. Asl and A. Mahloojifar, "Minimum variance beamforming combined with adaptive coherence weighting applied to medical ultrasound imaging," *IEEE Trans. Ultrason., Ferroelectr., Freq. Control*, vol. 56, no. 9, pp. 1923–1931, Sep. 2009, doi: 10.1109/TUFFC.2009.1268.
[37] Z. Lan, L. Jin, S. Feng, C. Zheng, Z. Han, and H. Peng, "Joint generalized coherence factor and minimum variance beamformer for synthetic aperture ultrasound imaging," *IEEE Trans. Ultrason., Ferroelectr., Freq. Control*, vol. 68, no. 4, pp. 1167–1183, Apr. 2021, doi: 10.1109/TUFFC.2020.3035412.
[38] B. Hu, X. J. Li, and P. H. J. Chong, "Denoised modified incoherent signal subspace method for DOA of coherent signals," in *Proc. IEEE Asia–Pacific Conf. Antennas Propag. (APCAP)*, Auckland, New Zealand, Aug. 2018, pp. 539–540, doi: 10.1109/APCAP.2018.8538143.
[39] J. Zheng, N. Tagawa, M. Yoshizawa, and T. Irie, "Super-resolution plane wave beamforming based on frequency and angle compound," in *Proc. 43th Symp. Ultrason. Electron.*, Kyoto, Japan, Nov. 2022, pp. 1–2, Paper 3Pb2-3, doi: 10.24492/use.43.0_3Pb2-3.
[40] Y. Saito and N. Tagawa, "One-shot beam-forming with adaptively weighted compound of multiple transmission angles and subbands," *Jpn. J. Appl. Phys.*, vol. 61, pp. 1–9, Jun. 2022, Art. no. SG1079, doi: 10.35848/1347-4065/ac6e26.
[41] H. Hasegawa and R. Nagaoka, "Converting coherence to signal-to-noise ratio for enhancement of adaptive ultrasound imaging," *Ultrason. Imag.*, vol. 42, no. 1, pp. 27–40, Dec. 2019, doi: 10.1177/0161734619889384.
[42] Y. Chen, D. Chen, T. Jiang, and L. Hanzo, "Channel-covariance and angle-of-departure aided hybrid precoding for wideband multiuser millimeter wave MIMO systems," *IEEE Trans. Commun.*, vol. 67, no. 12, pp. 8315–8328, Dec. 2019, doi: 10.1109/TCOMM.2019.2942307.
[43] B. Luijten, R. Cohen, F. J. de Bruijn, H. A. W. Schmeitz, M. Mischi, Y. C. Eldar, and R. J. G. van Sloun, "Adaptive ultrasound beamforming using deep learning," *IEEE Trans. Med. Imag.*, vol. 39, no. 12, pp. 3967–3978, Dec. 2020, doi: 10.1109/TMI.2020.3008537.
[44] A. Wiacek, E. Gonzalez, and M. A. L. Bell, "CohereNet: A deep learning architecture for ultrasound spatial correlation estimation and coherence-based beamforming," *IEEE Trans. Ultrason., Ferroelectr., Freq. Control*, vol. 67, no. 12, pp. 2574–2583, Dec. 2020, doi: 10.1109/TUFFC.2020.2982848.

**JIE ZHENG** received the M.E. degree from the Graduate School of Systems Design, Tokyo Metropolitan University, Japan, in 2021, where he is currently pursuing the Ph.D. degree. His research interests include medical ultrasound, ultrasound imaging, signal processing, and deep learning.

**JING ZHU** received the Ph.D. degree in division of information and communications systems engineering from Tokyo Metropolitan University, Japan, in 2019. She is currently an Assistant Research Fellow with the Research Institute of Intelligent Sensing, Zhejiang Laboratory, Hangzhou, China. Her research interests include industrial ultrasound, medical ultrasound, ultrasound imaging, signal processing, and machine learning.

**NORIO TAGAWA** (Member, IEEE) received the M.E. degree from the Tokyo Institute of Technology, Yokohama, Japan, in 1989, and the D.E. degree from Tokyo Metropolitan University, Tokyo, Japan, in 1995. He joined Fujitsu Laboratories Ltd., Kawasaki, Japan, in 1989. He is currently a Professor with the Department of Electrical Engineering and Computer Science, Tokyo Metropolitan University. His research interests include computational vision, statistical signal processing, and ultrasonic engineering.